Materials & Design 208 (2021) 109863

Contents lists available at ScienceDirect

Materials & Design

journal homepage: www.elsevier.com/locate/matdes

Energy absorption and self-sensing performance of 3D printed CF/PEEK cellular composites

J. Jefferson Andrew [b], Hasan Alhashmi [b], Andreas Schiffer [b], S. Kumar [a,b,*], Vikram S. Deshpande [c]

[a] James Watt School of Engineering, University of Glasgow, Glasgow G12 8QQ, UK
[b] Department of Mechanical Engineering, Khalifa University, P.O. Box 127788, Abu Dhabi, United Arab Emirates
[c] Department of Engineering, University of Cambridge, Trumpington Street, Cambridge CB2 1PZ, UK

HIGHLIGHTS

- Multifunctional CF/PEEK lattices processed via FFF is reported.
- CF/PEEK lattices exhibit 20X increase in peak stress and 5X increase in SEA.
- The piezoresistive response of CF/PEEK lattices is more sensitive to cell-topology.
- CF/PEEK lattices show the highest sensitivity of 5.2 under out-of-plane compression.

GRAPHICAL ABSTRACT

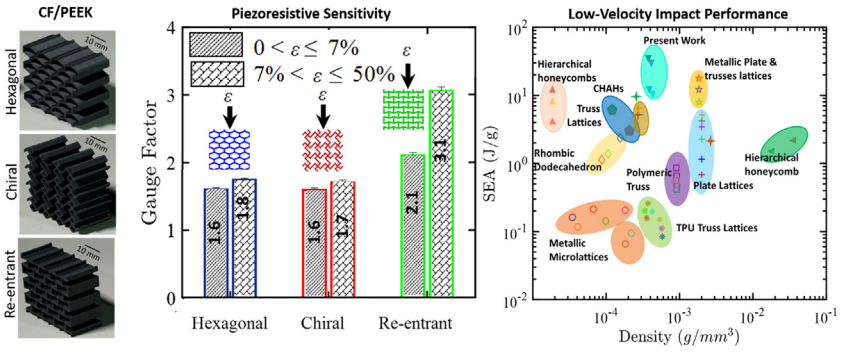

ARTICLE INFO

Article history:
Received 13 February 2021
Revised 25 May 2021
Accepted 31 May 2021
Available online 1 June 2021

Keywords:
3D Printing
Honeycomb lattices
Low-velocity impact
Piezoresistive self-sensing
CF/PEEK cellular composites

ABSTRACT

We report the energy absorption and piezoresistive self-sensing performance of 3D printed discontinuous carbon fiber (CF)-reinforced polyetheretherketone (PEEK) cellular composites. Experiments conducted on three different 2D lattices with hexagonal, chiral and re-entrant topologies of the same relative density (33%) and CF loading (30 wt%) reveal that the CF/PEEK hexagonal lattice (HL), due its relatively brittle response, shows about 40% and 9% decrease in specific energy absorption (SEA) under in-plane and out-of-plane compression, respectively, compared with PEEK HL. While the collapse response of PEEK HL is nearly insensitive to the strain-rate over $43 \leq \dot{\varepsilon} \leq 106$ s^{-1}, we observe a twenty-fold increase in peak stress and a five-fold increase in SEA under in-plane impact loading over the same range of strain-rates for the CF/PEEK HL. The CF/PEEK lattices exhibit pronounced piezoresistive response under both in-plane and out-of-plane compression with maximum sensitivity of 3.1 and 5.2, respectively, for the re-entrant lattice, offering insight into the damage-state. Higher damage sensitivity indicates faster percolation of new contacts due to folds forming between the cell walls within the lattice under compression. The energy-absorbing and strain- and damage-sensing nature of 3D printed CF/PEEK lattices demonstrated here offers insight into the design of lightweight, high-performance multifunctional lattices.

1. Introduction

Cellular materials are abundantly available in nature and have inspired the creation of intriguing material architectures with optimal mechanical and functional performance [1]. These materials

* Corresponding author at: James Watt School of Engineering, University of Glasgow, Glasgow G12 8QQ, UK.
E-mail address: s.kumar@eng.oxon.org (S. Kumar).

https://doi.org/10.1016/j.matdes.2021.109863
0264-1275/

comprise periodic or stochastic arrangement of unit cells in 2D or 3D space [2], and their macroscopic properties can be tailored by tuning the architectural features at the *meso*-scale (unit-cell level). Tailorability of lattice materials (cellular materials with periodic array of unit cells) makes them suitable candidates for a broad range of engineering applications. Several studies have examined the effect of cell topology considering a wide range of unit cell geometries (e.g. corrugated lattices, honeycombs, truss-lattices, plate-lattices, auxetics, etc.) on the mechanical response of lattice structures [3]. Among various types of lattice structures, 2D lattices (also commonly known as "honeycombs") have been extensively studied and used as a stiff and lightweight core material for sandwich structures in a broad range of applications [4]. A considerable amount of effort has been dedicated to examining the energy absorption characteristics of 2D lattices under compressive in-plane and out-of-plane loads using experimental, numerical, and theoretical approaches [5].

In recent years, the development of high-performance lightweight lattices with multifunctional attributes has attracted considerable attention in the research community [6,7]. These novel materials are seen as critical enablers for advanced structural applications that possess not only high specific strength, specific stiffness, toughness and durability, but also offer additional functionalities enabled by their electrical, magnetic, thermal, or chemical properties [8]. Multifunctionality is often engineered into the structural systems through incorporation of nanomaterials such as carbon nanotubes, graphene etc [7] in the polymer matrix. These nanofillers offer the ability to sense structure's deformation- and/or damage-state induced by operational or accidental loading, often facilitated by its piezoresistive property, which allows the material to alter its electrical resistance with applied strain [9,10]. Such electro-conductive polymer nanocomposites are promising candidates for self-sensing applications since they can be processed into complex shapes at a relatively lower cost [11], and their properties can be readily tuned to the demands of a particular application [12]. The piezoresistive characteristics of nanofillers incorporated composites are primarily governed by contact resistance change between fillers, tunnelling resistance change between neighbouring fillers and resistance change due to microcracking of the matrix [7,13]. On the other hand, discontinuous micro-scale carbon fibers are often used as reinforcements in thermoplastic polymer-based lattice structures, in which the carbon fibers not only provide enhanced mechanical characteristics, but also form an electrical percolation network. The electrical resistance of the composites changes with applied strain, thereby offering piezoresistive-sensing capability [14–16]. Hence, the integration of high-performance carbon fibers in a polymer matrix is a reasonable strategy for building mechanically robust and self-sensing lattice structures. The choice of unit-cell architecture and material system for a particular application necessitates a careful balance of mechanical and functional attributes, cost, and durability as well as quasi-static and dynamic failure characteristics. However, the integration of an optimized material system in a complex structural configuration across various length scales is difficult to achieve with conventional manufacturing techniques.

In recent years, additive manufacturing (AM) has attracted considerable interest from the research community and has become the leading processing technique for complex 3D lattice structures [17–19]. The most common AM methods are fused filament fabrication (FFF), stereolithography (SLA), binder jetting (BJ), multijet fusion (MJF), selective laser sintering (SLS), selective laser melting (SLM), electron beam melting (EBM), electron beam additive manufacturing (EBAM) and big area additive manufacturing (BAAM) [20]. Each AM process has its distinctive merits and is suitable for the fabrication of a specific family of materials. Polyether ether ketone (PEEK), a semi-crystalline thermoplastic polymer, is widely being used in applications that demand high chemical resistance, thermal stability [21] and mechanical strength [22]. Fabrication of PEEK has been explored both via FFF and SLS techniques. PEEK enabled by FFF was shown to exhibit tensile strengths of up to 83–98 MPa, which are higher than those of samples fabricated via SLS (80–90 MPa) [23]. Moreover, FFF of PEEK has attracted extensive attention due to its cost-effectiveness [24,26]. However, its high melting temperature (340 °C) and melt viscosity (350 Pa s) make the fabrication far more challenging [38] and therefore careful selection of the process parameters is crucial for achieving good print-quality [25]. The high melting temperature of PEEK requires nozzle temperatures in excesses of 360 °C, which decreases the porosity of fabricated components and increases the crystallinity, resulting in enhanced mechanical properties [27]. Furthermore, FFF allows to combine different phases (e.g., fibre and matrix) in the AM process, providing the opportunity for tailoring the mechanical and functional properties [28,29] of resulting composites. Carbon fibres (CF) reinforced PEEK composites are extensively being considered for lightweight structural applications often attracted by the recyclability of high temperature thermoplastic PEEK resin and multifunctional properties of CF. Carbon fibers possess excellent thermal and electrical conductivity in addition to their superior mechanical characteristics [30]. The key mechanisms that govern the piezoresistive response of CF reinforced polymer composites are: (i) change in contact resistance between CF [13], (ii) the disruption in electrical paths due to microcracking in the matrix [31] and (iii) the change in resistance of the CF mainly due to dimensional change rather than resistivity change [13]. In this study, we make use of the change in electrical resistance of CF-reinforced PEEK composites to enable piezoresistive *in situ* strain- and damage-sensing of CF/PEEK of cellular composites [32]. The incorporation of discontinuous CF in the PEEK matrix would not only enhance the mechanical characteristics of the 3D printed CF/PEEK lattices but also provide piezoresistive self-sensing capability [33].

The practical application of lattice structures in energy absorbing systems requires knowledge of the effect of strain-rate on their mechanical performance [34]. Some types of lattices are vulnerable to damage under impact loading, causing partial or total loss of functionality and structural integrity [35]. The strain-rate sensitivity of lattice materials typically arises due to a combination of various factors, such as the micro-inertial effect [35], the strain-rate dependence of the baseline material, the flow and compression of air locked in unit-cells, the occurrence of shock waves, the structural architecture, and the length-scale of the structure [36]. Previous studies reported that the impact resistance of lattice structures increased between 20 and 703 % at impact velocities of around 30 m s^{-1}, due to the formation of shock waves in the lattice. Other authors related the improvements in strength and energy absorption under dynamic loading to the occurrence of strain localization in the lattice structure [37–39]. Although the strain-rate dependence of various types of 3D printed lattice structures has been studied in the recent literature, only limited information is available on the response of PEEK lattices processed via FFF, mainly due to the difficulties involved in processing these structures via extrusion-based AM methods. Furthermore, there is a lack of information on how the incorporation of micro-scale carbon fibers in the PEEK matrix influences the mechanical and piezoresistive response of 3D printed lattice structures.

In this study, we experimentally demonstrate the mechanical and piezoresistive characteristics of short carbon fiber-reinforced PEEK lattices processed via FFF and provide detailed insight into the rate-dependent mechanical behavior and quasi-static self-sensing characteristics of CF/PEEK cellular composites. The effects of different unit-cell geometries and material systems to the applied strain-rate were examined by comparing the energy

absorbing characteristics of the structures under quasi-static and low-velocity impact conditions [40]. Three different 2D lattices with hexagonal, chiral and re-entrant topologies of the same relative density (33%) and CF loading (30 wt%) were considered. Initially, we performed a series of in-plane and out-of-plane quasi-static compression tests on each type of lattice to characterize their compressive response and identify active failure modes. Subsequently, we measured the compressive in-plane and out-of-plane responses of the three 3D-printed lattices under elevated rates of strain by performing low-velocity impact tests. Furthermore, we evaluated the self-sensing characteristics of the electro-conductive CF/PEEK lattices under quasi-static compression. To the best of our knowledge, this paper is the first to examine the in-plane and out-of-plane mechanical responses of CF/PEEK 2D lattices processed via FFF additive manufacturing. It also breaks new ground in providing detailed information on the piezoresistive self-sensing characteristics of CF/PEEK 2D lattices, relating them to their underlying deformation modes and damage.

2. Experimental procedure

2.1. Materials

The neat polyether ether ketone (PEEK) and carbon fiber-reinforced polyether ether ketone (CF/PEEK) filaments of diameter 1.75 mm (supplied by Apium Additive Technologies GmbH, Germany) were used as feedstock. The CF/PEEK filaments consisted of 30 wt% discontinuous carbon fibers of approximately 2–3 μm diameter and 100–150 μm length, according to the datasheet, and this was also confirmed via Scanning Electron Microscopy, as shown in Fig. S1 (Supplementary Information). The mechanical properties of the neat PEEK and the CF/PEEK filaments are summarized in Table S3 (Supplementary Information).

2.2. Fabrication of lattices via 3D printing

A fused filament fabrication (FFF) 3D printer, Apium P220 (Apium Additive Technologies GmbH, Germany), was employed to fabricate the PEEK and CF/PEEK 2D lattice structures. Simplify 3D software (version 3.0.4.6114) was used to set the printing parameters and generate the G-Code required for the FFF process. The printing process parameters (see, Table S4), were chosen as per the recommendation of the materials supplier. The most commonly used 2D non-auxetic (hexagonal) and auxetic (chiral, and re-entrant) honeycomb structures were chosen for the investigation (see, Fig. 1). Choice of these topologies would facilitate a comprehensive assessment of the associated effects of the geometrical features and materials systems on the deformation mechanisms of honeycomb structures at different loading rates. For each cell topology, multiple lattice structures were 3D printed via FFF using both the neat PEEK and CF/PEEK filaments (see Fig. 2). The PEEK and CF/PEEK filaments were dried at 120 °C for 12 h to remove moisture prior to 3D printing. The printing orientations were chosen by considering the practical build-envelope of our 3D printer. The sample was printed in such a way that the boundary with the largest surface area seated on the print bed. All the lattice structures were printed with the same orientation to avoid differences in mechanical performance related to printing orientation since the mechanical properties of the 3D printed parts are print-orientation dependent.

Each lattice structure consists of 4 × 4-unit cells with equal overall dimension (40 mm × 40 mm × 20 mm) and relative density (33%). Note that all unit-cell geometries (see Fig. 1) had the same in-plane size of 10 mm × 10 mm, and the dimensions of the structural features of each unit cell are listed in Table S5. The selection of the unit-cell size was guided by the results obtained from test prints which showed that the minimum thickness of the ligaments is 1.12 mm for the relative density chosen here (33%). While this is larger than the resolution of the 3D printer (0.5 mm), we noticed several defects in the 3D printed geometric features smaller than 1.12 mm due to several factors [41,42]. The average measured densities of the 3D printed hexagonal, chiral and re-entrant PEEK lattices were 420, 393 and 460 kg m^{-3} and those of the CF/PEEK lattices were 406, 390 and 438 kg m^{-3} respectively. Although the CF/PEEK filaments had a higher density than the neat PEEK filaments, the 3D printed CF/PEEK lattices exhibit a lower average density, suggesting that the CF/PEEK composite lattice has a significant porosity often concentrated between the beads [41,42].

2.3. Quasi-static compressive testing

Quasi-static compression tests (standard ASTM C365 / C365M – 16) were perfromed on an MTS electronic universal testing machine (UTM) equipped with a load cell of 300 kN. The honeycomb samples were placed between two circular hardened steel platens and compressed at a crosshead speed of 5 mm/min. Optical images of all the quasi-static tests were acquired by a conventional Nikon D5300 DSLR camera with 256 × 112 pixels and at a rate of 40–50 μs/frame. Note that the tests were also performed on 3D printed bulk samples to measure basic mechanical properties of the neat PEEK and CF/PEEK under uniaxial compression, tension and in three-point bending, as detailed in Section S1.2 (Supplementary Material). For each configuration, three samples were tested to confirm the repeatability of our measurements.

2.4. Low velocity impact testing

Low-velocity impact tests (standard ASTM 7136/D7136M) were conducted on the honeycomb lattices using a CEAST Fractovis drop weight impact tester. The impact set-up includes a drop-weight impactor, an anti-rebounding mechanism, a rigid base, and a guide mechanism. A high-speed Vision Research Phantom camera was employed to record the deformation sequences at a frame rate of 35,000 fps. The high-speed images were used to observe the deformation process and to identify dynamic failure mechanisms. To prevent multiple impacts, an anti-rebounding mechanism was activated after the end of the first impact. A dynamic load cell of 50 kN load capacity was employed to acquire the impact load-time history during the impact event. The impact tester was equipped with an infrared sensor to measure the velocity vs. time history of the impactor. The lattice structures were placed on a rigid flat base, and the samples were crushed under uniaxial compression by a flat-faced impactor of 60 mm diameter. Both in-plane and out-of-plane impact tests were conducted for each 2D lattice structure considered here, and the impact height, mass, velocity and energy used in the in-plane and out-of-plane tests are listed in Table 1 and Table 2, respectively. For each testing condition, three samples were tested. A CEAST DAS 64 k digital data acquisition system was used to acquire the time histories of contact force, velocity, energy, and displacement at a signal sampling frequency of 3 MSPS (Million Samples per Second).

The time histories of absorbed energy were measured from the acquired force, velocity and time data according to Newton's second law [43]

$$\delta(t) = \delta_i + v_i t + \frac{gt^2}{2} - \int_0^t \left[\int_0^{t'} \frac{F(t'')}{m} dt' \right] dt \tag{1}$$

$$E_a(t) = \frac{1}{2} m \left[{v_i}^2 - {v_f}^2(t) \right] + mg\delta(t) \tag{2}$$

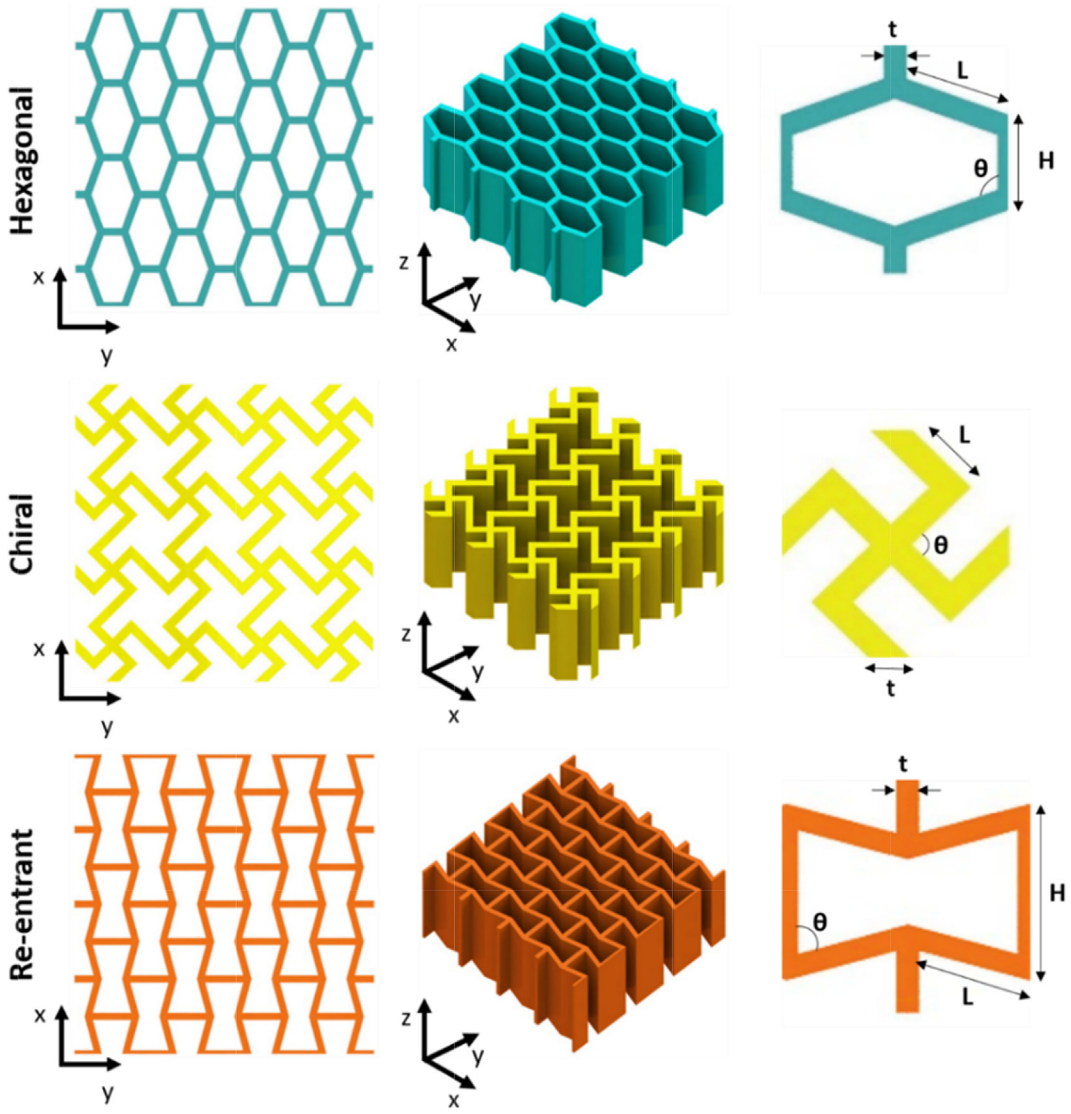

Fig. 1. Geometric models of the 2D lattices: hexagonal (top row), chiral (middle row) and re-entrant (bottom row) lattices, all with solid volume fraction (relative density), $\bar{\rho}$ = 33%. The architectural parameters are given in Table S5.

where δ is the striker displacement, δ_i is the initial position of the striker, v_i is the initial velocity, v_f is the final velocity, m is the striker mass, F is the contact force and $E_a(t)$ is the absorbed energy at time t.

2.5. Piezoresistance measurements under quasi-static compression

The piezoresistive responses of the CF/PEEK lattice structures were measured *in situ* using a DMM 4050 (Tektronix, USA) digital multimeter (see Fig. S3, Supplementary Information). The multimeter has a range between 10 Ω and 1 GΩ for resistance measurement with a resolution of 10 μΩ. The samples are electrically insulated from the UTM to prevent any influence on resistance measurement by leakage of electrical charge. For each test, the measured change in resistance, $\Delta R = R - R_0$, normalized by the initial no-load resistance R_0, $\Delta R/R_0$, was plotted against the applied strain ε, and the obtained data was used to evaluate the gauge factor k, defined as the slope of the $\Delta R/R_0$ vs. ε curve within the initial linear piezoresistive regime [44]:

$$k = \frac{\Delta R/R_0}{\Delta \varepsilon} \tag{3}$$

Prior to testing, CF/PEEK samples were treated with concentrated sulfuric acid (H_2SO_4, 95–97%) to etch the surface of CF/PEEK composite that is covering the carbon fibers and expose the conductive network. The samples were then soaked and rinsed with distilled water, and dried in a furnace at 70 °C. For each sample configuration, three samples were tested. We note that the latter treatment did not cause any major damage to the carbon fibers or the internal morphology of the structures, which was apparent from the SEM micrographs illustrated in Fig. S4 (Supplementary Information). The depth of the pores produced by acid treatment was on the order of tens of micrometers [42] (i.e., < 1 print layer thickness of 100 μm).

3. Results and discussion

3.1. Energy absorption characteristics of PEEK and CF/PEEK lattices under quasi-static compression

3.1.1. In-plane response

Fig. 3a shows the nominal stress–strain responses of the neat PEEK lattices of hexagonal, chiral and re-entrant topology under

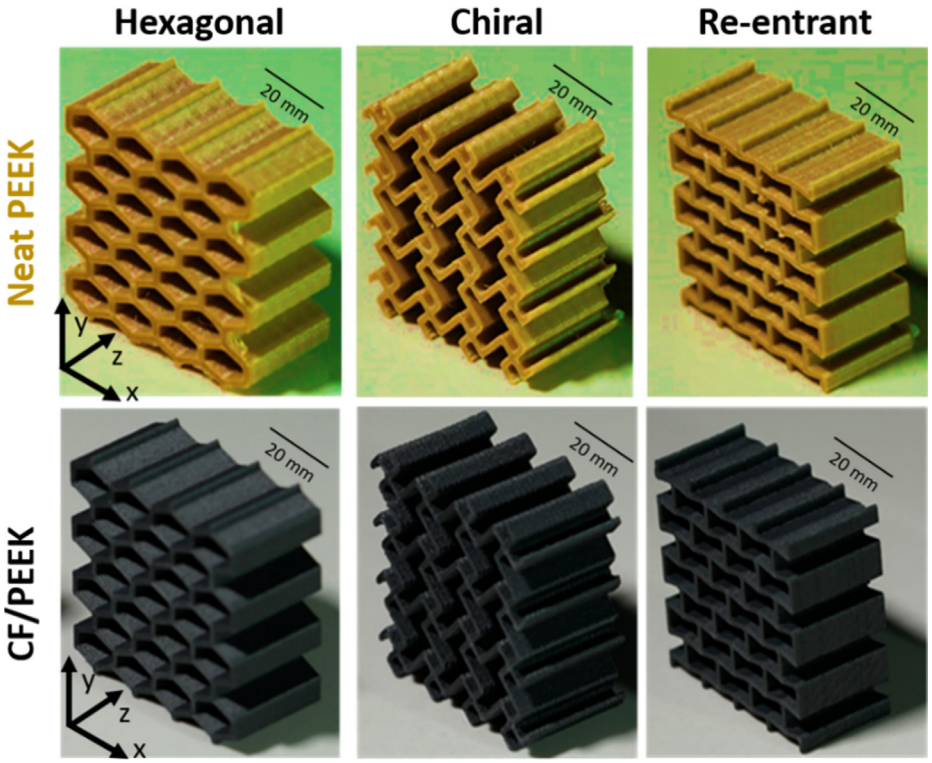

Fig. 2. Additively manufactured neat PEEK (top row) and CF/PEEK (bottom row) lattice structures with hexagonal, chiral and re-entrant unit cell-topologies.

Table 1
Summary of impact height, mass, velocity and impact energy chosen for in-plane impact tests.

Impact mass (kg)	Impact Height (mm)	Impact Velocity (m s^{-1})	Impact Energy (J)	Average Strain-Rate (s^{-1})
16.75	152	1.7	25	43
16.75	304	2.4	50	61
16.75	609	3.5	100	86
16.75	913	4.2	150	106

Table 2
Summary of impact height, mass, velocity and energy chosen for out-of-plane impact tests.

Impact mass (kg)	Impact Height (mm)	Velocity (m s^{-1})	Impact Energy (J)	Average Strain-Rate (s^{-1})
18.6	549	3.3	100	164
28.4	717	3.8	200	188
37.0	829	4.0	300	201
46.9	870	4.1	400	207

in-plane quasi-static compression along with *in situ* deformation maps captured at different stages of loading. The stress–strain responses exhibit three sequential stages: (i) an initial linear elastic region; (ii) a stress plateau with superimposed stress fluctuations in which the cell walls collapse gradually and (iii) progressive strain hardening caused by densification of the cellular structures. From Fig. 3a, it is clear that the collapse response is sensitive to the unit-cell topology. For the re-entrant lattice, the collapse of cell walls commences with a sharp drop in stress without any noticeable prior plastic deformation (see top row of Video SV1, Supplementary Information). The corresponding images recorded from this test show that the collapse response is triggered by elastic buckling of cell walls within a horizontal array of cells, through which plastic deformation and failure processes advance rapidly.

We further note that the re-entrant lattice is known to be auxetic at low compressive strains [45] and this behavior causes lateral compression in the angled bend-dominated cell walls, promoting an unstable response, as observed here. When the strain is further increased, the re-entrant lattice undergoes a layer-by-layer collapse process (see images B-C), which results in additional stress fluctuations before densification commences [46]. In contrast, the chiral lattice shows a blunt peak at a relatively low stress level followed by a small drop in stress and a subsequent strain-hardening phase. In the latter hardening phase, cell walls start to rotate about plastic hinges formed in the lattice, resulting in increased contact between adjacent cell walls and the formation of additional load transfer paths (see images B-C). It is also seen from the recorded images (B-C), that the chiral lattice rotates (or distorts) significantly during the collapse phase, due to co-operative rotation of vertical cell arrays in clockwise direction.

Among all lattices shown in Fig. 3a, the (non-auxetic) hexagonal lattice shows the highest, longest and most stable plateau region in which only minor stress fluctuations are observed. The recorded images (A-C) show that the stretch-dominated vertical members

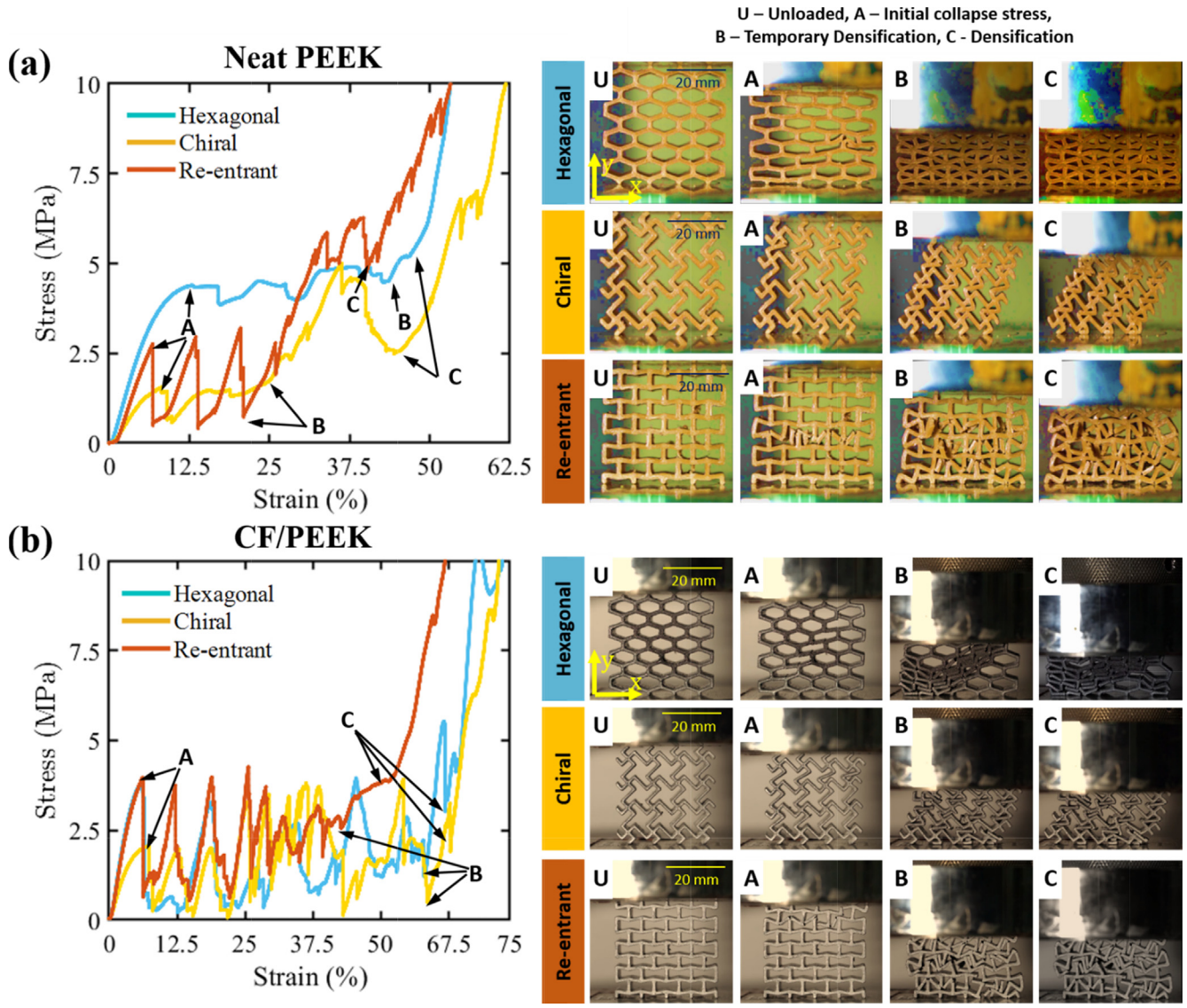

Fig. 3. In-plane quasi-static compression behavior of different 2D lattices (see Video SV1): Characteristic stress–strain curves of (a) neat PEEK and (b) CF/PEEK lattices with hexagonal, chiral and re-entrant unit-cell geometry. For each type of lattice, a deformation map at various stages of the response is provided. Zoomed images are provided in the Supplementary Information (see Fig. S8).

of the hexagonal lattice are sufficiently short to resist sudden failure of inclined ligaments (predominantly) via elastic buckling, and therefore no significant load drops are observed. It is also seen from images B-C, that the hexagonal lattice folds into a fully stretch-dominated triangular lattice, enabled by the formation of plastic hinges at the nodal points of the lattice structure. This transition from a bend-dominated to a stretch-dominated lattice is manifested, in the stress–strain response, by a steep increase in hardening modulus at the onset of densification, which occurs at a larger compressive strain as compared to the re-entrant lattice. The latter observation can be explained by the fact that the hexagonal honeycomb expands laterally during compression while the auxetic re-entrant lattice tends to pull the cell walls inwards, which, in turn, causes early densification.

The stress–strain responses and deformation sequences of different CF/PEEK lattices are presented in Fig. 3b. The stress–strain curves of all CF/PEEK lattices (see Fig. 3b and bottom row of Video SV1, Supplementary Information) show stress fluctuations with significant load drops during the collapse phase. The recorded images (see Fig. 3b) show that the collapse mechanisms of the CF/PEEK re-entrant and chiral lattices are qualitatively similar to their PEEK counterparts. However, significant differences are observed for the hexagonal honeycomb lattice, where a shear band is formed at a strain of approximately 7% (see Fig. 3b). Compared to the respective neat PEEK lattices, the hexagonal lattice is the only CF/PEEK lattice to show an initial collapse at a lower strain level, whereas the other two auxetic lattices start to collapse almost at the same strain. During the collapse phase, the occurrence of outward hinge rotation (lateral direction) along with the lower ductility of the CF/PEEK composite (see Fig. S2, Supplementary Information) might have led to the premature collapse of the hexagonal lattice at the interface between the vertical and angled members, which, in turn, resulted in the formation of a diagonal shear band of the kind previously reported for similar lattice structures [47]. The latter strain localization phenomenon causes the stress to drop substantially during compression, and is not observed for the neat PEEK hexagonal lattice, which deforms more uniformly (see Fig. 3a). Furthermore, the higher level of inter-bead porosity in the CF/PEEK lattices, as inferred from their μCT images in Fig. S5 (see Supplementary Information) further induces the pre-

mature onset of failure. On the other hand, the constrained hinge-rotation of the auxetic lattices along with the higher intrinsic modulus of the CF/PEEK (see Table S2, Supplementary Information) might have led to the higher initial collapse stress compared to the respective neat PEEK lattices.

In Fig. 4, we compare the elastic modulus, initial collapse stress, specific energy absorption (SEA), and densification strain (ε_d) for all PEEK and CF/PEEK lattices considered here under in-plane quasi-static compression. Note that the densification strain,ε_d, indicated in Fig. 4d is the strain at which the stress reaches a value of 10 MPa during the densification stage, and the SEA was calculated from the obtained stress–strain responses via [48]:

$$SEA = \frac{1}{\rho}\int_0^{\varepsilon_d} \sigma d\varepsilon \tag{4}$$

where ρ is the average density of the lattice structure.

Fig. 4a shows that the elastic moduli of all CF/PEEK lattices are higher than those of PEEK counterparts, confirming that the carbon fibers have reinforcing effect on the in-plane response of the composite lattices. It is also seen from Fig. 4a that the moduli of the re-entrant and hexagonal lattices are similar in magnitude, which can be explained by the fact that the two lattices have a comparable amount of stretch-dominated, vertical lattice members [1], offering maximum resistance to axial compression. Since stretch-dominated members are absent in the chiral lattices, their moduli were found to be considerably lower than those of the hexagonal and re-entrant lattices. Moreover, the chiral lattices exhibit the lowest initial collapse stress among all three lattice topologies examined here, as seen from Fig. 4b, due to early formation of plastic hinges which leads to nonlinearities in the stress–strain responses triggered by large rotations of the cell walls (see Fig. 3a and b). The neat PEEK hexagonal lattice showed the highest resistance against plastic collapse, reporting an initial collapse stress of 4.4 MPa, even higher than that of the stiffer CF/PEEK lattice which showed premature collapse due to shear band formation (see Fig. 3b).

Fig. 4c shows that the neat PEEK hexagonal lattice outperforms all other lattices in terms of SEA, thanks to its uniform and stable collapse response (see Fig. 3a). The non-auxetic hexagonal lattice enables the best balance amid the stiffness and absorbed energy properties that are normally antagonistic. The global deformation in the outward lateral direction constrains premature initial collapse at the interfaces, unlike re-entrant lattice, while the presence of a larger volume of vertical cell walls restricts extensive straining, unlike the bending-dominant chiral lattice. The SEA of the hexagonal lattice drops from 5.6 to 3.4 J/g (~40%) with the incorporation of CF in neat PEEK, due to shear band formation observed during compression of the composite lattice (see Fig. 3b). It is also clear from Fig. 4c that the neat PEEK lattices have higher SEA than their CF/PEEK counterparts which can be explained by the higher ductility of the neat PEEK, as seen from *Fig. S2a* (Supplementary Information), resulting in higher capacity to absorb energy by plastic dissipation.

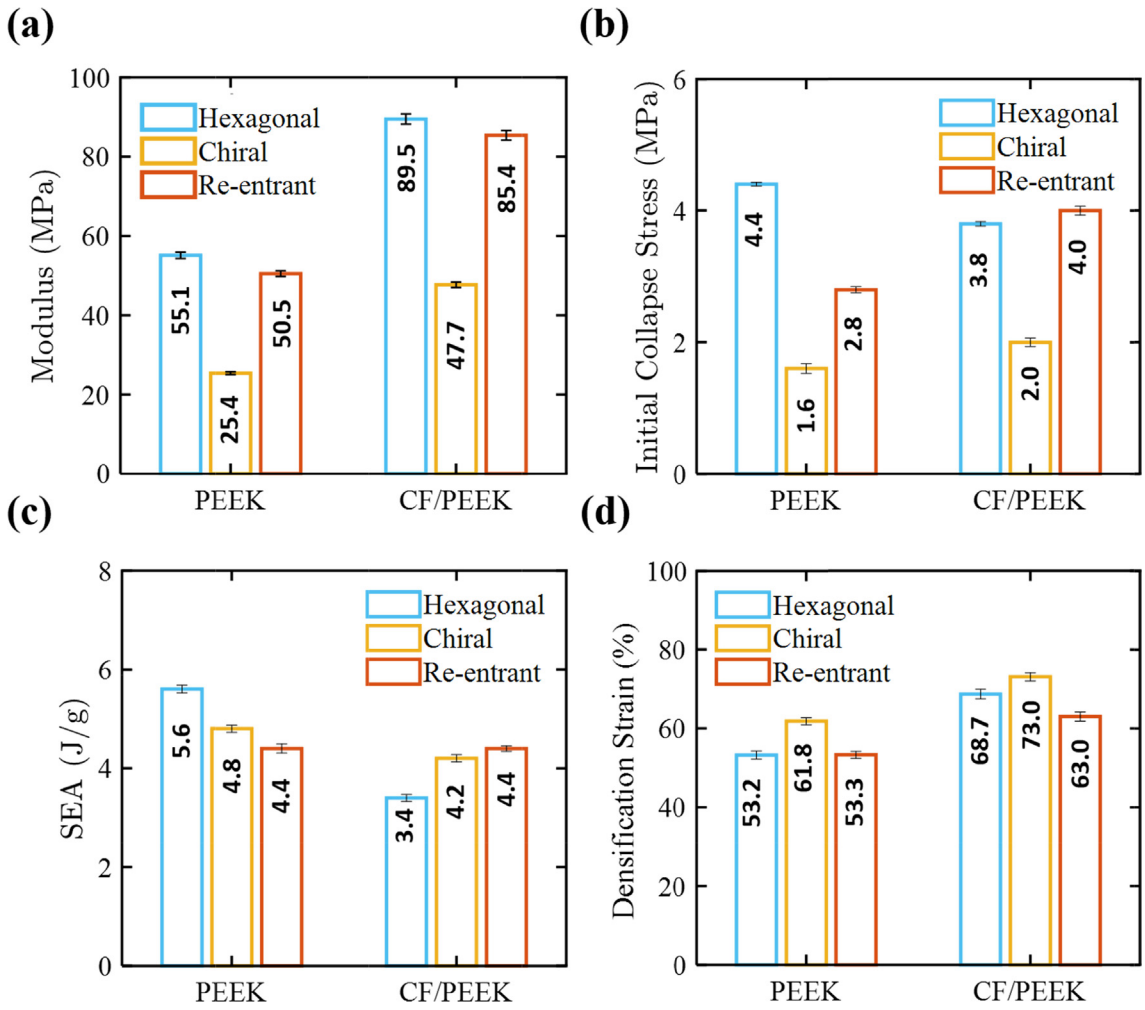

Fig. 4. In-plane mechanical characteristics of neat PEEK and CF/PEEK 2D lattices under quasi-static compression: (a) modulus, (b) initial collapse stress (the initial collapse stress of the lattices with blunt peak is measured at 5% plastic strain), (c) specific energy absorption, and (d) densification strain.

In Fig. 4d we plot the densification strains deduced from the data in Fig. 3, showing that the chiral lattice possesses the highest densification strain among the three unit-cell geometries. This can be explained by the fact that the chiral lattice rotates during collapse (see Fig. 3), and this allows the material to spread across a wider area, which delays the onset of densification. Densification occurs at higher strains for the CF/PEEK, due to the occurrence of brittle fracture in the lattice walls, allowing for denser packing of material as the lattice collapses (see Fig. 3b).

3.1.2. Out-of-plane response

Fig. 5 presents the nominal stress–strain responses of neat PEEK (Fig. 5a and top row of Video SV2, Supplementary Information) and CF/PEEK (Fig. 5b and bottom row of Video SV2) lattices under out-of-plane quasi-static compression, along with photographic images captured at different stages of loading. The stress–strain responses of neat PEEK and CF/PEEK lattices show qualitatively similar characteristics, and there are no significant differences between the responses of hexagonal, chiral and re-entrant lattices, confirming the topology-independent compressive response of honeycombs of the same relative density and basis material [18]. Following an initial linear elastic response, all lattices show a well-defined yield point beyond which a significant drop in stress is observed due to the onset of global cell wall buckling, as seen from the recorded images.

Densification of the lattices commences at a strain of 60–70% when the folded cell walls come into contact, resulting in a steep increase in stress with increasing compressive strain [46]. The photographic images in Fig. 5 and Video SV2 (Supplementary Information) show that the buckling of both the hexagonal and re-entrant lattices is associated with lateral bulging of the cell walls, while the dominant buckling mode of the chiral lattice is S-shaped which appears to limit lateral expansion during compression and forces the cell walls to fold inwards. This is evident from the post-mortem photographs presented in *Fig. S6* (Supplementary Information), where the re-entrant and hexagonal lattices show a larger cross-sectional area than the chiral ones after the lattices have fully densified. We note that the peak at around 45% strain for the re-entrant structure might be due to the temporary densification of cell walls [49].

Fig. 6 presents the elastic modulus, initial collapse stress, SEA and densification strain deduced from the stress–strain curves shown in Fig. 5. Since the 2D lattices are much stronger in the out-of-plane direction than in the in-plane direction, the densifica-

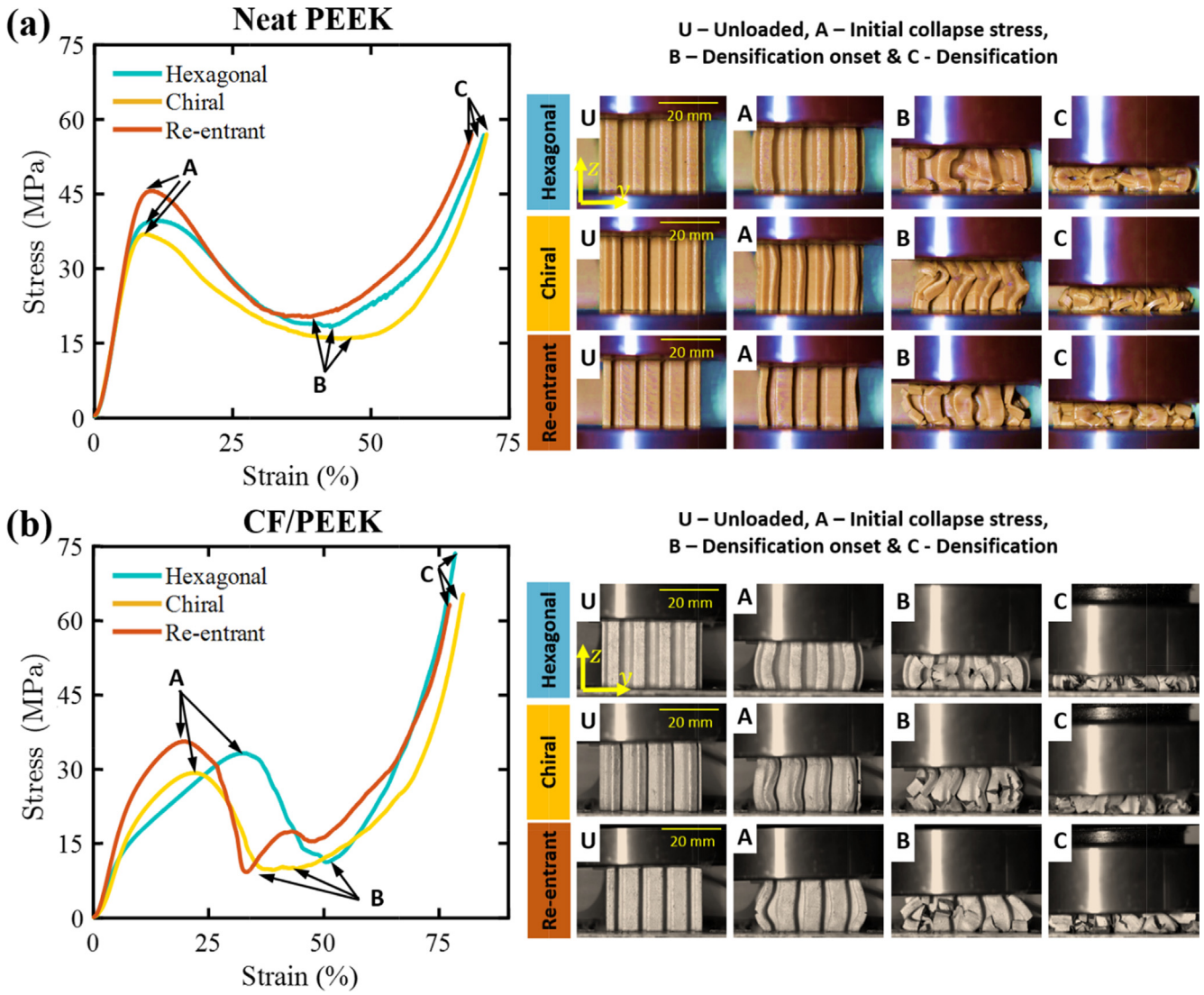

Fig. 5. Out-of-plane quasi-static compressive response of different 2D lattices (see Video SV2, Supplementary Information): Characteristic stress–strain curves of (a) neat PEEK and (b) CF/PEEK lattices with hexagonal, chiral and re-entrant unit cell geometry. For each type of lattice, a deformation map of the specimen at various stages of the response is provided. Zoomed images are provided in the Supplementary Information (see Fig. S9).

tion strain was taken here as the strain at which the stress reached a value of 60 MPa during compression, and the corresponding SEA was evaluated using eq. (4). It is evident from Fig. 6a that the CF/PEEK composite lattices have significantly lower modulus than their neat PEEK counterparts. This trend is opposite to what was observed in Fig. 4a for in-plane compression and can be explained by the fact that the carbon fibers tend to get aligned in the plane of printing (*x*-*y* plane in this case) along the printing direction as we build all the lattices layer-by-layer in *x*-*y* plane (see SEM images in Fig. S7, Supplementary Information), and therefore, carbon fibers in all the walls of the lattices are not subjected to its stronger stretching mode of deformation under out-of-plane compression as the short fibers in *x*-*y* plane at any *z*-location are perpendicular to out-of-plane direction. The exact orientation of fibers in the *x*-*y* plane is dictated by the orientation of inclined ligaments with respect to *x*- or *y*-direction. Furthermore, the CF/PEEK lattices show a higher level of inter-bead porosity due to unstable CF/PEEK melt flow through the nozzle during 3D printing, as inferred from their μCT images (see Fig. S5, Supplementary Information) and lower average densities, and this further lowers their stiffness in the out-of-plane direction. We note that the increased porosity in CF/PEEK might also be the reason for the more irregular patterns in the out-of-plane stress vs. strain responses between the three types of lattices, as observed from Fig. 5b. This stems from the difference in build-rate in *z*-direction for three different topologies. Moreover, Fig. 6a also shows that the out-of-plane moduli are only mildly sensitive to the cell geometry, which is expected since all cell walls are subjected to uniaxial compression in the initial elastic stage of deformation, regardless of the choice of cell geometry.

We observe from Fig. 6b that the chiral lattices exhibit the lowest initial collapse stress for both the neat PEEK and CF/PEEK composite, whereas the re-entrant lattices show the highest initial collapse stress. These differences can be attributed to variations in the buckling strength of the lattice members, which depends on the lattice height, the cell wall thickness, as well as on unit-cell size and geometry [50]. The collapse strengths of the CF/PEEK lattices are generally lower than those of neat PEEK lattices due to the lower out-of-plane modulus of the CF/PEEK lattices which limits the buckling strength of the cell walls and therefore leads to reduced collapse strength of the lattices. Fig. 6c shows that the neat PEEK hexagonal lattice possesses superior SEA as compared to all other types of lattices, similar to what was observed for in-plane compression (see Fig. 4c). It is also clear from Fig. 6c that the CF/PEEK lattices are marginally less effective in absorbing energy in the out of-plane direction as compared to the neat PEEK lattices, owing to the lower modulus and buckling strength of the CF/PEEK lattices. Fig. 6d shows that the CF/PEEK lattices have slightly higher densification strains than their neat PEEK counterparts, similar to what was observed under in-plane compression (see Fig. 4d).

3.2. Low-velocity impact response of PEEK and CF/PEEK lattices

In this section, we examine the energy-absorption characteristics of neat PEEK and CF/PEEK lattices subject to low-velocity impact loading, focusing on hexagonal honeycomb lattices, since they showed an overall better performance under both quasi-static in-plane and out-of-plane compression.

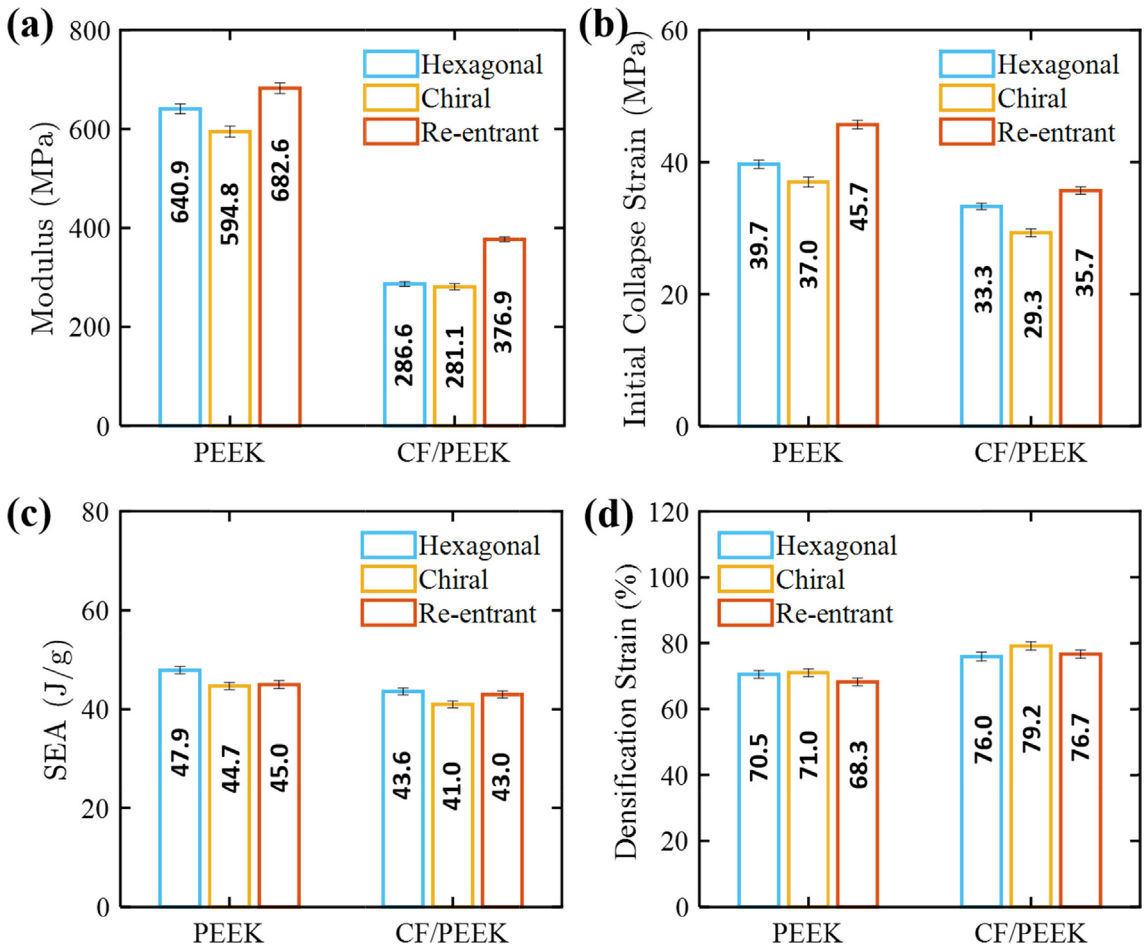

Fig. 6. Out-of-plane performance of neat PEEK and CF/PEEK 2D lattices under quasi-static compression: (a) modulus, (b) initial collapse stress (the initial collapse stress of the lattices with blunt peak is measured at 5% plastic strain from the stress–strain curves), (c) specific energy absorption, and (d) densification strain.

3.2.1. In-plane impact response

Fig. 7a presents the stress–strain responses and optical deformation maps captured at different strain levels of neat PEEK hexagonal lattice structures subject to impact loading in the in-plane direction over the strain-rates $43 \leq \dot{\varepsilon} \leq 106\ s^{-1}$ (see RHS top row of Video SV3, Supplementary Information). For $\dot{\varepsilon} \leq 61\ s^{-1}$, the samples only get crushed partially, and a small portion of the induced strain recovers by elastic spring back. For $\dot{\varepsilon} \geq 86\ s^{-1}$, we observe progressive strain hardening at the end of the stress plateau due to the densification of the honeycomb lattice. It is clear from Fig. 7a that the flow stress of the neat PEEK hexagonal lattice is nearly insensitive to the strain-rate for the ranges examined here, and the dynamic deformation mechanisms, observed during the impact, are similar to those shown in Fig. 3a for the case of quasi-static in-plane compression.

Fig. 7b shows similar information for the CF/PEEK hexagonal lattices. For $\dot{\varepsilon} \leq 61\ s^{-1}$, the dynamic stress–strain curves show pronounced stress fluctuations during the collapse phase with peak stresses ranging between 2 and 3 MPa, similar to what was observed for the quasi-static case (see Fig. 3b). At low strain rates (up to $61.08\ s^{-1}$), the interaction time between the impactor and the samples is longer (because the impactor moves slower), and the stress induced in the structure attains an equilibrium state during which the inertial effects are negligible. The corresponding high-speed deformation maps show evidence of the formation of shear bands, which grow in width as the sample continues to crush, analogous to what was observed in the quasi-static experiments. Due to the brittle nature of CF/PEEK, multiple peaks of similar amplitudes are observed in the stress–strain curves, which is a characteristic feature of a brittle cellular solid during the collapse phase.

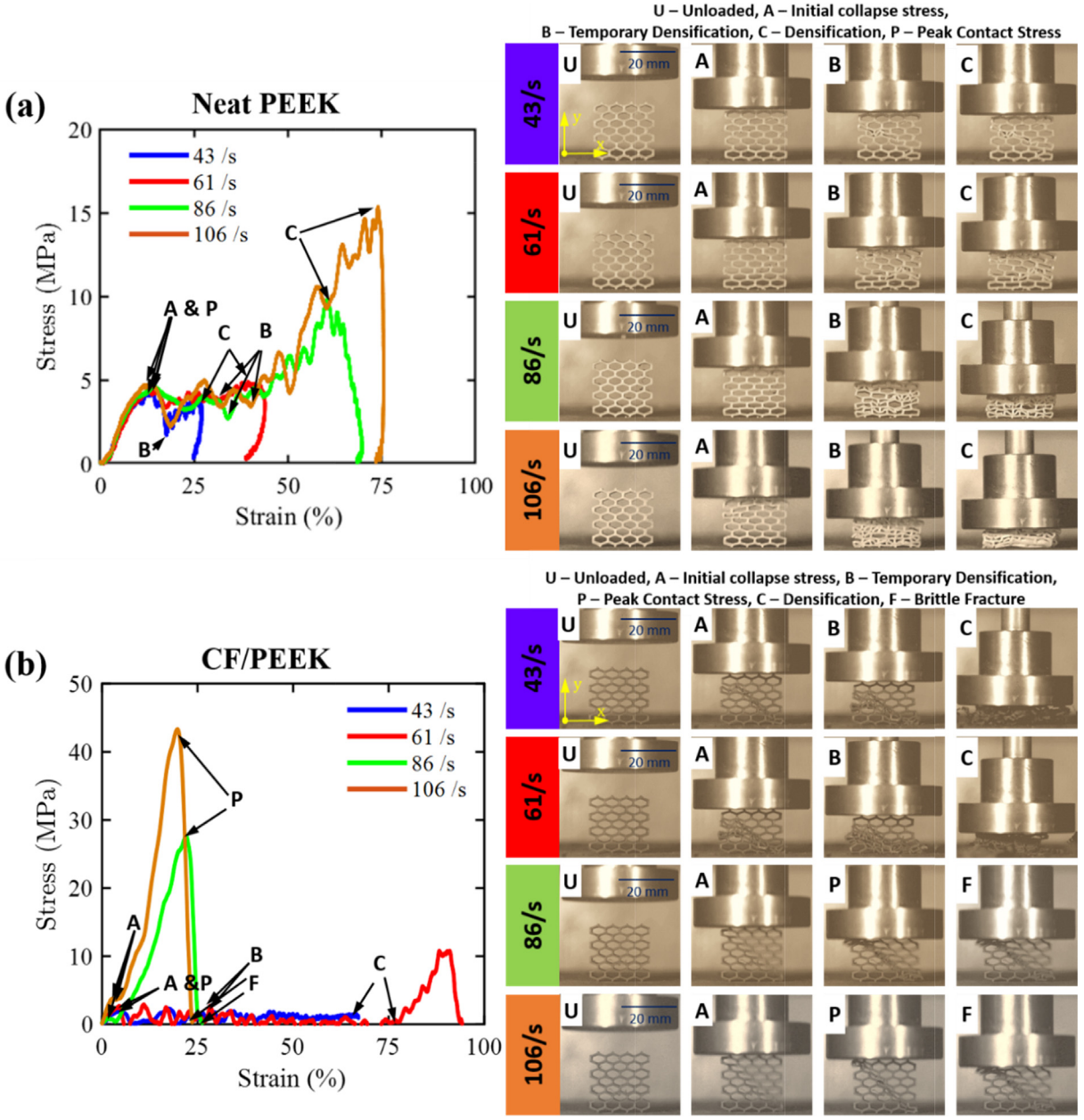

Fig. 7. In-plane impact response of hexagonal honeycomb lattices at different strain-rates (see RHS of Video SV3, Supplementary Information): Characteristic stress–strain curves of (a) neat PEEK and (b) CF/PEEK lattices. For each test, a high-speed image sequence is provided, showing the dynamic deformation of the specimen at various stages of loading. Zoomed images are provided in the Supplementary Information (see Figs. S10-S11).

At higher strain rates, $\dot{\varepsilon} \geq 86\ s^{-1}$, the stress–strain responses vary dramatically from the quasi-static case, exhibiting a short initial plateau region up to $\varepsilon \approx 5\%$, followed by a steep continuous hardening phase which terminates at the onset of brittle fracture at $\varepsilon \approx 25\%$, causing the stress to drop to zero instantaneously (see Fig. 7b) [46]. For $\dot{\varepsilon} \geq 86\ s^{-1}$, the peak stresses are approximately one order of magnitude larger than those measured in the plateau region with lower strain rates, $\dot{\varepsilon} \leq 61\ s^{-1}$. With regard to the underlying collapse mechanism of the CF/PEEK lattice loaded at $\dot{\varepsilon} \geq 86\ s^{-1}$, we observe, in Fig. 7b, the formation of a distinct shear band within which the strain localizes rapidly. It is also noticed that the unit cells outside the shear band maintained their hexagonal shape until the final stages of the collapse process, which is clearly different to the more uniform and progressive crushing of cell walls observed in Fig. 7b at lower strain rates (i.e. $\dot{\varepsilon} \leq 61\ s^{-1}$).

Previous studies have shown that the collapse of lattice structures is governed by micro-inertial dynamic effects when the strain-rate is high, resulting in non-uniform compression of the lattice, and this, in turn, leads to a pronounced hardening effect [35,36]. Based on these findings, it can be argued that effects of inertia have caused the CF/PEEK honeycomb to compress non-uniformly at elevated strain-rates, which results in the collapse stress to become proportional to the impact velocity (see, e.g., [51] for a detailed analysis), as observed here. The transition to an inertia-dominated collapse mode is not observed for the PEEK lattice (see Fig. 7a) for the range of $\dot{\varepsilon}$ examined here, and this can be attributed to various reasons, including the differences in the mechanical properties of PEEK and CF/PEEK (see Table S2, Supplementary Information) and possible differences in their strain-rate sensitivity (not evaluated in this work). However, it is expected that the neat PEEK lattice would exhibit dynamic effects in the collapse response at higher rates of strain than those examined here, i.e., $\dot{\varepsilon} > 106\ s^{-1}$. However, such high strain-rates could not be achieved with the specimen sizes and test equipment used in this work. It is also noted that all CF/PEEK lattices failed by brittle fracture and disintegrated completely over the entire range of strain-rates considered here (see Fig. 7b) (see RHS bottom row of Video SV3, Supplementary Information), while the neat PEEK lattices showed significant amount of plastic deformation which is evident from the folded cell walls shown in Fig. 7a.

From the dynamic stress–strain responses shown in Fig. 7a and b, we deduced the peak stresses in the collapse phase (i.e. excluding the densification stage) of neat PEEK and CF/PEEK honeycomb lattices, respectively, and the obtained results are plotted in Fig. 8a. For the case of neat PEEK, the peak stresses are only mildly sensitive to the strain-rate and approximately equal to the quasi-static peak stress (4.4 MPa, see Fig. 4b) which indicates that dynamic effects are negligible in the response of the PEEK honeycomb over the range of strain-rates considered here. For $\dot{\varepsilon} < 86\ s^{-1}$, the peak

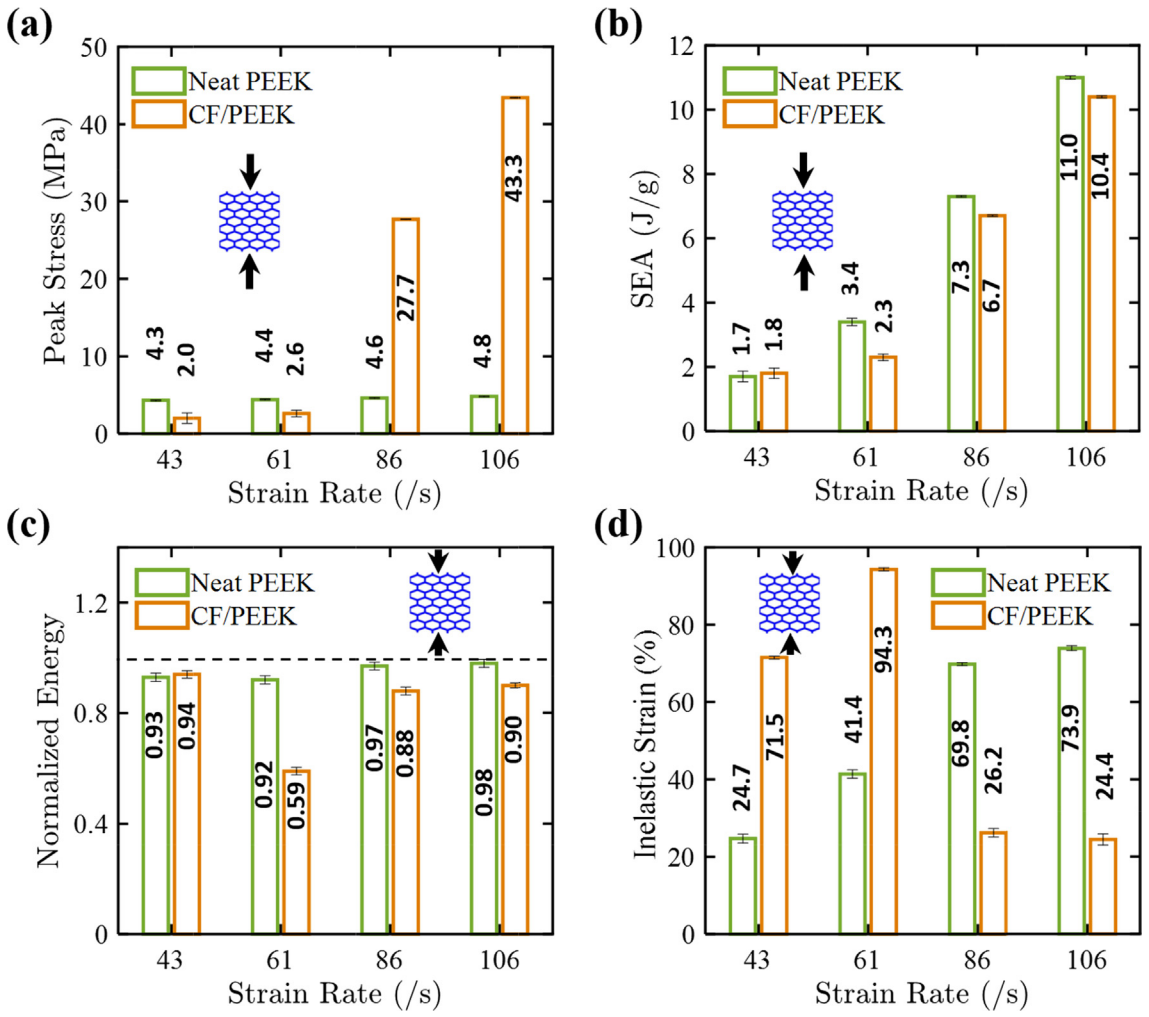

Fig. 8. In-plane impact response of neat PEEK and CF/PEEK hexagonal honeycomb lattices: (a) peak stress (the peak stress of the lattices with blunt peak is measured at 5% plastic strain from the stress–strain curves), (b) specific energy absorption, (c) normalized energy, and (d) inelastic strain.

stresses of the CF/PEEK lattices are smaller than those under quasi-static conditions (3.8 MPa, see Fig. 4c), while for higher strain-rates, the peak stresses increase substantially, exceeding the quasi-static peak stress by a considerable margin which can be explained by the fact that the collapse response of the CF/PEEK lattice becomes inertia-dominated at strain-rates between 61 and 86 s^{-1}, as discussed above. As effects of inertia become more dominant, the collapse stress is expected to increase with increasing impact speed [51], and this is reflected in Fig. 8a where the collapse stress of the CF/PEEK lattice increases with increasing strain rate. The rate-dependent elevation in peak stress results in a concomitant increase of in SEA for the CF/PEEK lattice, as seen from Fig. 8b, where the SEA is shown for different strain-rates, with the SEA defined as the total energy absorbed by the material upon the impact. The SEA of the CF/PEEK reached 10.4 J/g at $\dot{\varepsilon}$ = 106 s^{-1}, a five-fold increase as compared to the SEA value at $\dot{\varepsilon}$ = 43 s^{-1}. The SEA of the neat PEEK lattices also increased steadily with increase in strain-rate and was found to be slightly higher than that of the CF/PEEK lattices. Fig. 8c shows the rate-dependence of the normalized energy, defined as the ratio of the energy absorbed by the material to the energy of the impactor. The normalized energy of the neat PEEK lattice approaches a limiting value of 1 with increasing strain-rate, suggesting that nearly the entire impact energy was absorbed by the material. Since the CF/PEEK lattices failed by brittle fracture under impact loading, their normalized energies are not as high as those observed for the neat PEEK lattices. The inelastic strains induced in the neat PEEK and CF/PEEK lattices are plotted in Fig. 8d. For the case of neat PEEK, the inelastic strains increase monotonically with increasing strain-rate, as expected, reporting a maximum of 73.9% at $\dot{\varepsilon}$ = 106 s^{-1}. Similar trends were observed for the CF/PEEK lattices at lower strain rates, $\dot{\varepsilon} \leq$ 61 s^{-1}. It can also be seen that the inelastic strains induced in the CF/PEEK lattices are larger than those in the PEEK lattices due to the fact that the PEEK lattices collapse at higher stresses for $\dot{\varepsilon} \leq$ 61 s^{-1} (see Fig. 8a), offering higher resistance against impact deformation. However, at higher strain rates, $\dot{\varepsilon} \geq$ 86 s^{-1}, the inelastic strains induced in the CF/PEEK lattices are substantially smaller (only 24.4% at $\dot{\varepsilon}$ = 106 s^{-1}) than those measured under lower strain-rates, which can be attributed to the rapid increase in the collapse stress at higher strain rates (see Fig. 8a) where dynamic effects become dominant. These results allow concluding that the rate effects can play a vital role in the in-plane collapse response of CF/PEEK lattice structures and need to be considered when using such materials for impact and blast mitigation.

3.2.2. Out-of-plane impact response

Additional impact tests were performed to examine the out-of-plane response of the hexagonal honeycomb lattices at higher strain-rates. Measurements indicate that the SEA increases steadily with increasing strain-rate, although CF/PEEK lattices exhibit marginally higher SEA than the PEEK lattices. For more detailed discussion on the deformation characteristics of the honeycomb lattices at higher strain-rates, see the Supplementary Information, Section S3.

3.3. Piezoresistive response of CF/PEEK lattices under quasi-static compression

In Fig. 9a, we plot the measured normalized resistance change, $\Delta R/R_0$, as a function of the compressive strain applied in the in-plane direction of hexagonal, chiral and re-entrant lattices. It is seen from Fig. 9a and bottom row of Video SV1 (Supplementary Information) that $\Delta R/R_0$ decreases monotonically with increasing strain for all lattice architectures considered here. The reason for this can also be seen by observing the deformation modes seen in Video SV1: the relatively brittle CF/PEEK composite results in the collapse of the cells with compressive strain and the formation of crush bands. New contacts between struts of the lattices are created with the crush bands percolating across the specimen.

The percolated bands are pathways of low resistance and the source of the decreasing resistance [52]. With increasing compressive strain, more and more percolated crush bands form which finally results in near complete loss of electrical resistance of the crushed lattices. Therefore, the piezoresistive responses at higher strains, become non-linear, approaching a limiting value of $-\Delta R/R_0 = 1$ at a strain of around ε = 65%, where the lattices approach full densification (see Fig. 3b), causing the electrical resistance R to become vanishingly small. We emphasize here that this large change (~100%) in the electrical resistance is not associated with the bending deformation of the cell walls. To clarify this, observe that the resistance of the CF/PEEK bulk material increases with increasing bending deformation (albeit by only 15% or so; see *Fig. S2c*, Supplementary Information).

We also note that the lattices show a linear piezoresistive response over a small strain range of $\varepsilon \leq$ 7%, which relates to the linear elastic regime of the response (also see, Fig. 3b). The corresponding gauge factors (strain sensitivity), evaluated in the initial linear portion of the curve according to eq. (3) are included in Fig. 9b with values k = 1.64, 1.60 and 2.05 for hexagonal, chiral and re-entrant lattices, respectively. The piezoresistive response transitions from linearity to non-linearity when in-elastic deformation of lattices commences. The average gauge factors evaluated in the non-linear regime over 7% < $\varepsilon \leq$ 50% for hexagonal, chiral and re-entrant lattices are 1.8, 1.7 and 3.1, respectively, as shown in Fig. 9b. Although, gauge factors of different topologies in non-linear regime exhibit a similar trend as in linear regime, k in this regime is dependent upon the rate of collapse of cells and percolation of crush bands across the specimen. The gauge factor k in this regime offers insight into damage-state; higher values of k (re-entrant, in this case) indicate faster percolation of crush bands within the lattice.

Fig. 9c presents the measured $\Delta R/R_0$ vs. strain response for the same types of lattices subjected to quasi-static out-of-plane compression (see bottom row of Video SV2, Supplementary Information). The piezoresistive response of the all three lattices are less pronounced under out-of-plane compression compared to that under in-plane compression. In the small strain regime, the $\Delta R/R_0$ values increase with increasing compressive strain, while we observe decreasing $\Delta R/R_0$ values for larger strains. Now unlike in the in-plane compression case, this decrease is via a combination of the decrease in the resistance of the cell wall material under compression (see *Fig. S2*a, Supplementary Information) and the formation of new contacts due to folds forming between the cell walls as seen in Video SV2. We argue that the initial increase in electrical resistance is associated with the lateral expansion of the cell walls (qualitatively similar to bulk samples under compression, see *Fig. S2*a) in the elastic regime of the response, due to partial breakage of the conductive path induced by the Poisson's effect. The corresponding gauge factors evaluated in the falling and rising branches of the $\Delta R/R_0$ vs. ε curve, respectively, are plotted in Fig. 9d, showing that the gauge factors are larger, in magnitude, in the large strain regime (indicating damage-state) than in the initial elastic regime of the response (indicating strain-state). The figure also shows that, under out-of-plane compression, the re-entrant lattice exhibits the highest gauge factor (in magnitude) of k = 5.2, followed by the chiral and hexagonal lattices with k = 4.9 and k = 3.2, respectively, and the initial gauge factors show similar trends. Compared to the case of in-plane compression (Fig. 9b), the gauge factors measured under out-of-plane compression (Fig. 9d) are relatively more sensitive to the lattice geometry. This stems from the difference in deformation modes of the lattices under

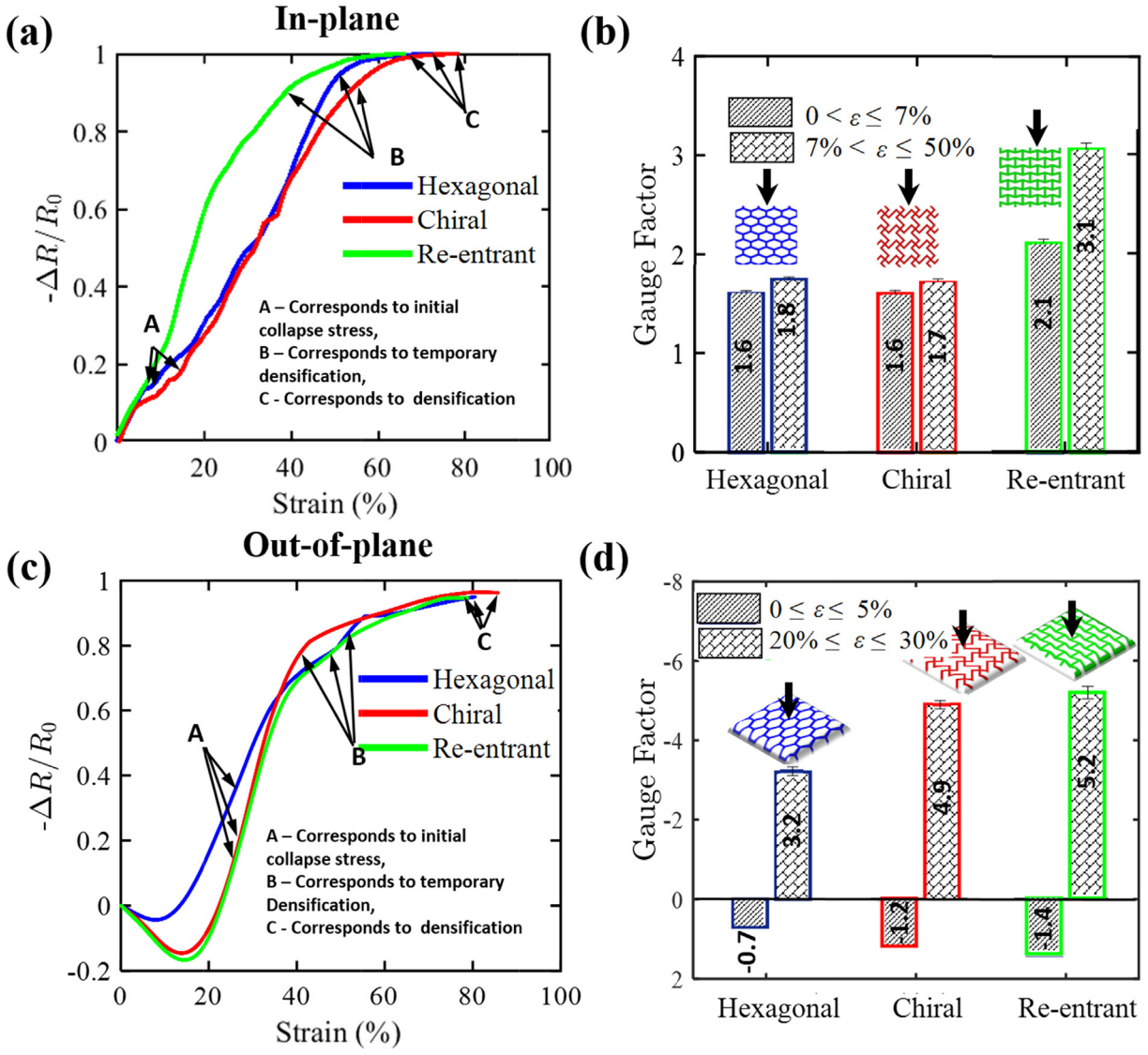

Fig. 9. Piezoresistive response of CF/PEEK lattices with hexagonal, chiral and re-entrant cell-topology under quasi-static compression: (a) normalized change in resistance as function of in-plane compressive strain (see bottom row of Video SV1, Supplementary Information); (b) gauge factor for in-plane compression evaluated within $\varepsilon \leq 7\%$ and over $7\% < \varepsilon \leq 50\%$; (c) normalized change in resistance as a function of out-of-plane compressive strain (see bottom row of Video SV2); (d) gauge factor for out-of-plane compression evaluated within $\varepsilon \leq 5\%$ (−ve) and over $20\% \leq \varepsilon \leq 30\%$.

in-plane compression (Fig. 3) and that under out-of-plane compression (Fig. 5) as discussed earlier. Finally, we note that the gauge factors of piezoresistive thermoplastic composites under uniaxial compression often range between 1 and 7, according to previous studies [53], which agree reasonably well with the results presented in Fig. 9.

4. Conclusions

In this study, we examined the energy absorption and/or piezoresistive self-sensing characteristics of AM-enabled PEEK and CF/PEEK lattices under quasi-static compression and impact loading. Three different 2D PEEK and CF/PEEK lattices with hexagonal, chiral and re-entrant topologies were 3D printed via fused filament fabrication technique. Each type of CF/PEEK lattice comprised 30 wt% of discontinuous carbon fibers with a relative density of 33%. The effect of strain-rate on mechanical response, active failure modes and the piezoresistive characteristics of AM-enabled lattices subjected to quasi-static compression and/or low-velocity impact loading were examined. The measured mechanical characteristics of the CF/PEEK lattices were compared to those of neat PEEK lattices of the same relative density (33%).

Under in-plane quasi-static compression, the elastic moduli of the CF/PEEK lattices were found to be significantly higher than those of the neat PEEK lattices, due to the reinforcing effect provided by the embedded carbon fibers. Opposite trends were observed under out-of-plane compression, where the moduli of the CF/PEEK lattices dropped well below their neat PEEK counterparts. This decrease is primarily attributed to the fact that the carbon fibers in all the walls of the lattices are not subjected to their stronger stretching mode of deformation under out-of-plane compression as the short fibers in *x*-*y* plane at any *z*-location are perpendicular to out-of-plane direction. The neat PEEK hexagonal lattice showed the most stable collapse response under in-plane loading, and outperformed all other lattices in terms of specific energy absorption (SEA) with SEA = 5.6 J/g. The SEA values of the CF/PEEK lattices under in-plane loading were found to be lower than those of the neat PEEK lattices, due to the relatively brittle behavior of the CF/PEEK composite. This behaviour is attributed

to premature fracture of cell walls and their inability to absorb energy by plastic dissipation. The effect of unit-cell topology on the collapse response of the lattice was much less pronounced under out-of-plane compression where lattice collapse was triggered by global buckling of the cell walls, which caused the stress to drop significantly during compression for both the CF/PEEK and neat PEEK lattices. Again, the highest SEA under out-of-plane compression was found for the neat PEEK hexagonal lattice, reporting SEA = 47.9 J/g.

The low-velocity impact tests showed that under in-plane loading, the collapse response of the neat PEEK hexagonal lattice is nearly insensitive to the strain-rate over $43 \leq \dot{\varepsilon} \leq 106\ s^{-1}$. For the CF/PEEK hexagonal lattice, on the other hand, we observed a twenty-fold increase in the flow stress over the same range of strain-rates, suggesting that the collapse process of this type of lattice is controlled by dynamic effects at elevated strain-rates that result in non-uniform lattice compression. It was also found that the neat PEEK hexagonal lattices were able to absorb the entire impact energy under in-plane loading while the more brittle CF/PEEK lattices fractured during the test after the formation of a shear band, and therefore, absorbed a slightly smaller fraction of the impact energy. Under out-of-plane impact loading, both neat PEEK and CF/PEEK lattices showed similar performances, however, the CF/PEEK lattice responded to the impact with higher inelastic deformations, indicating lower resistance against impact damage.

Although the neat PEEK lattice showed superior energy absorption characteristics than their CF/PEEK counterparts under quasi-static compression, the existence of a significant weight percentage of electrically conductive short carbon fibers in the non-conducting PEEK matrix results in a conductive CF/PEEK composite, whose resistance changes with applied deformation, resulting in multi-functional lattices with piezoresistive sensing capability. The nearly topology-independent piezoresistive response observed under in-plane compression of CF/PEEK lattices is governed by the formation of percolated crush bands, leading to near complete loss (−100%) of electrical resistance of the crushed lattices. On the other hand, the topology-dependent piezoresistive response under out-of-plane compression, is governed by a combination of the decrease in the resistance of the cell wall material under compression and the formation of new contacts due to folds forming between the cell walls, eventually leading to a ~95% decrease in electrical resistance of crushed lattices. Furthermore, it was demonstrated that the CF/PEEK lattices exhibit pronounced piezoresistive behavior under both in-plane and out-of-plane compression, with maximum gauge factors of k = 3.1 and 5.2, respectively, signifying the damage sensitivity of the re-entrant lattice (which showed the highest sensitivity among all lattice topologies considered here). These multifunctional carbon fiber-reinforced cellular composites have the potential to become critical enablers for smart structural systems capable of *in situ* sensing of strain and/or damage induced by operational or accidental loads.

Declaration of Competing Interest

The authors declare that they have no known competing financial interests or personal relationships that could have appeared to influence the work reported in this paper.

Acknowledgements

SK would like to thank the University of Glasgow for the start-up grant [award no: 144690-01]. Authors would like to acknowledge the funding provided by Khalifa University through the Competitive Internal Research Award (CIRA) [grant number: CIRA-2018-128]. Authors thank Mr. Johannes Schneider, University of Glasgow for his help in creating videos, and Mr. Pradeep George, Khalifa University for assisting with the micro-CT scans.

Appendix A. Supplementary material

Supplementary data to this article can be found online at https://doi.org/10.1016/j.matdes.2021.109863.

References

[1] T. Tancogne-Dejean et al., 3D plate-lattices: an emerging class of low-density metamaterial exhibiting optimal isotropic stiffness, Adv. Mater. 30 (45) (2018) 1803334.
[2] X. Yu et al., Mechanical metamaterials associated with stiffness, rigidity and compressibility: a brief review, Prog. Mater Sci. 94 (2018) 114–173.
[3] H. Lei et al., Evaluation of compressive properties of SLM-fabricated multi-layer lattice structures by experimental test and μ-CT-based finite element analysis, Mater. Des. 169 (2019) 107685.
[4] J. Schneider et al., Energy absorption characteristics of additively manufactured plate-lattices under low-velocity impact loading, Int. J. Impact Eng. (2020) 103768.
[5] Z. Dong et al., Experimental and numerical studies on the compressive mechanical properties of the metallic auxetic reentrant honeycomb, Mater. Des. 182 (2019) 108036.
[6] S. Yuan, C.K. Chua, K. Zhou, 3D-printed mechanical metamaterials with high energy absorption, Adv. Mater. Technol. 4 (3) (2019) 1800419.
[7] J. Li et al., Recent progress in flexible and stretchable piezoresistive sensors and their applications, J. Electrochem. Soc. 167 (3) (2020) 037561.
[8] R. Gibson, A review of recent research on mechanics of multifunctional materials and structures, Compos. Struct. 92 (2010) 2793–2810.
[9] S. Kumar, T.K. Gupta, K.M. Varadarajan, Strong, stretchable and ultrasensitive MWCNT/TPU nanocomposites for piezoresistive strain sensing, Compos. B Eng. 177 (2019) 107285.
[10] J. Teixeira et al., Piezoresistive response of extruded polyaniline/(styrene-butadiene-styrene) polymer blends for force and deformation sensors, Mater. Des. 141 (2018) 1–8.
[11] B.F. Gonçalves et al., Green solvent approach for printable large deformation thermoplastic elastomer based piezoresistive sensors and their suitability for biomedical applications, J. Polym. Sci., Part B: Polym. Phys. 54 (20) (2016) 2092–2103.
[12] J.R. Dios et al., Piezoresistive performance of polymer-based materials as a function of the matrix and nanofiller content to walking detection application, Compos. Sci. Technol. 181 (2019) 107678.
[13] N. Kalashnyk et al., Strain sensing in single carbon fiber epoxy composites by simultaneous in-situ Raman and piezoresistance measurements, Carbon 109 (2016) 124–130.
[14] M.F. Arif et al., Strong linear-piezoresistive-response of carbon nanostructures reinforced hyperelastic polymer nanocomposites, Compos. A Appl. Sci. Manuf. 113 (2018) 141–149.
[15] Y. Liu, B. Zwingmann, M. Schlaich, Carbon fiber reinforced polymer for cable structures—a review, Polymers 7 (2015) 2078–2099.
[16] T.K. Gupta et al., Self-sensing and mechanical performance of CNT/GNP/UHMWPE biocompatible nanocomposites, J. Mater. Sci. 53 (11) (2018) 7939–7952.
[17] J.J. Andrew et al., Impact performance enhancement of honeycombs through additive manufacturing-enabled geometrical tailoring, Int. J. Impact Eng. 134 (2019) 103360.
[18] S. Kumar et al., Tunable energy absorption characteristics of architected honeycombs enabled via additive manufacturing, ACS Appl. Mater. Interfaces 11 (45) (2019) 42549–42560.
[19] P. Köhnen et al., Mechanical properties and deformation behavior of additively manufactured lattice structures of stainless steel, Mater. Des. 145 (2018) 205–217.
[20] D. Feeney, FFF vs. SLA vs. SLS: 3D Printing. 3D Printing, Rapid Prototyping 2019. Available from: https://www.sd3d.com/fff-vs-sla-vs-sls/.
[21] J.K. Fink, 3 – Epoxy Resins, in: J.K. Fink (Ed.), Reactive Polymers: Fundamentals and Applications, third ed., William Andrew Publishing, 2018, pp. 139–223.
[22] F. Voulpiotis, 3D Printing Materials: PEEK, ULTEM and other High Performance Polymers, 2019. Available from: https://www.3dnatives.com/en/3d-materials-peek-ultem-170120194/.
[23] L.J. Tan, W. Zhu, K. Zhou, Recent progress on polymer materials for additive manufacturing, Adv. Funct. Mater. 30 (43) (2020) 2003062.
[24] A. Stepashkin et al., 3D-printed PEEK-Carbon Fiber (CF) composites: structure and thermal properties, Compos. Sci. Technol. 164 (2018).
[25] P. Geng et al., Effects of extrusion speed and printing speed on the 3D printing stability of extruded PEEK filament, J. Manuf. Processes 37 (2019) 266–273.
[26] A.R. Rajkumar, K. Shanmugam, Additive manufacturing-enabled shape transformations via FFF 4D printing, J. Mater. Res. 33 (24) (2018) 4362–4376.
[27] S. Yuan et al., Polymeric composites for powder-based additive manufacturing: materials and applications, Prog. Polym. Sci. 91 (2019) 141–168.
[28] J.M. Chacón et al., Additive manufacturing of continuous fibre reinforced thermoplastic composites using fused deposition modelling: effect of process

parameters on mechanical properties, Compos. Sci. Technol. 181 (2019) 107688.
[29] M.A. Caminero et al., Impact damage resistance of 3D printed continuous fibre reinforced thermoplastic composites using fused deposition modelling, Compos. B Eng. 148 (2018) 93–103.
[30] D.D. Chung, Self-monitoring structural materials, Mater. Sci. Eng.: R: Rep. 22 (2) (1998) 57–78.
[31] X. Wang, S. Wang, D. Chung, Sensing damage in carbon fiber and its polymer-matrix and carbon-matrix composites by electrical resistance measurement, J. Mater. Sci. 34 (11) (1999) 2703–2713.
[32] P. Conor, C. Owston, Electrical resistance of single carbon fibres, Nature 223 (5211) (1969) 1146–1147.
[33] S. Blazewicz, B. Patalita, P. Touzain, Study of piezoresistance effect in carbon fibers, Carbon 35 (10) (1997) 1613–1618.
[34] T. Fíla et al., Dynamic impact testing of cellular solids and lattice structures: application of two-sided direct impact Hopkinson bar, Int. J. Impact Eng. 148 (2021) 103767.
[35] S. McKown et al., The quasi-static and blast loading response of lattice structures, Int. J. Impact Eng. 35 (8) (2008) 795–810.
[36] Y.D. Liu et al., A numerical study on the rate sensitivity of cellular metals, Int. J. Solids Struct. 46 (22) (2009) 3988–3998.
[37] P.J. Tan et al., Dynamic compressive strength properties of aluminium foams. Part I—Experimental data and observations, J. Mech. Phys. Solids 53 (10) (2005) 2174–2205.
[38] J.J. Andrew et al., Parameters influencing the impact response of fiber-reinforced polymer matrix composite materials: a critical review, Compos. Struct. 224 (2019) 111007.
[39] L. Verma et al., Compression after ballistic impact response of pseudoelastic shape memory alloy embedded hybrid unsymmetrical patch repaired glass-fiber reinforced polymer composites, J. Compos. Mater. 53 (28–30) (2019) 4225–4247.
[40] Y. Duan et al., Quasi-static and dynamic compressive properties and deformation mechanisms of 3D printed polymeric cellular structures with Kelvin cells, Int. J. Impact Eng. 132 (2019) 103303.
[41] M.F. Arif et al., Performance of biocompatible PEEK processed by fused deposition additive manufacturing, Mater. Des. 146 (2018) 249–259.
[42] M.F. Arif et al., Multifunctional performance of carbon nanotubes and graphene nanoplatelets reinforced PEEK composites enabled via FFF additive manufacturing, Compos. B Eng. 184 (2020) 107625.
[43] A. Arteiro et al., Low velocity impact and flexural performance of sandwich structures with cork and polymer foam cores, Ciência Tecnologia dos Materiais 25 (2) (2013) 79–84.
[44] P. Verma, A. Schiffer, S. Kumar, Thermo-resistive and thermo-piezoresistive sensitivity of carbon nanostructure engineered thermoplastic composites processed via additive manufacturing, Polym. Test. 93 (2021) 106961.
[45] X.-T. Wang et al., Mechanical properties of 3D re-entrant auxetic cellular structures, Int. J. Mech. Sci. 131 (2017) 396–407.
[46] Y. Zhang et al., Static and dynamic crushing responses of CFRP sandwich panels filled with different reinforced materials, Mater. Des. 117 (2017) 396–408.
[47] X. Liu et al., Understanding and suppressing shear band formation in strut-based lattice structures manufactured by laser powder bed fusion, Mater. Des. 199 (2021) 109416.
[48] P.H. Thornton, Energy absorption in composite structures, J. Compos. Mater. 13 (3) (1979) 247–262.
[49] J.J. Andrew, P. Verma, S. Kumar, Impact behavior of nanoengineered, 3D printed plate-lattices, Mater. Des. 202 (2021) 109516.
[50] Q. Liu et al., Axial and lateral crushing responses of aluminum honeycombs filled with EPP foam, Compos. B Eng. 130 (2017) 236–247.
[51] V.S. Deshpande, N.A. Fleck, One-dimensional response of sandwich plates to underwater shock loading, J. Mech. Phys. Solids 53 (11) (2005) 2347–2383.
[52] A. Mora, P. Verma, S. Kumar, Electrical conductivity of CNT/polymer composites: 3D printing, measurements and modeling, Compos. B Eng. 183 (2020) 107600.
[53] F. Avilés et al., Effect of carbon nanotube length on the piezoresistive response of poly (methyl methacrylate) nanocomposites, Eur. Polym. J. 110 (2019) 394–402.